PHYSICAL REVIEW APPLIED **10,** 014022 (2018)

Performance Projections for Two-dimensional Materials in Radio-Frequency Applications

Sukhwinder Singh, Kartikey Thakar, Naveen Kaushik, Bhaskaran Muralidharan, and Saurabh Lodha[*]
Department of Electrical Engineering, IIT Bombay, Powai, Mumbai 400076, India

(Received 11 August 2017; revised manuscript received 2 April 2018; published 23 July 2018)

Given the immense attraction of using two-dimensional materials for high-frequency applications, there is a critical need for computational models that aid the production of high-frequency performance projections based on their material properties. In this work, we use the atomistic nonequilibrium Green's function approach to predict the performance of ballistic radio-frequency transistors based on a broad range of two-dimensional semiconducting materials, including MoS_2, WS_2, WSe_2, and phosphorene. Self-consistent ballistic quantum-transport simulations are performed on monolayer transistors with a 15-nm gate length and an effective gate-oxide thickness of 0.44 nm. We show that rather than the bandgap, the effective mass and the dielectric constant significantly influence the unity current gain cutoff frequency (f_t), the maximum oscillation frequency ($f_{\max}$), and the intrinsic gain (G_{int}). Phosphorene with a low effective mass and high dielectric constant is found to be the most promising material with $f_t \simeq 10$ THz, $f_{\max} \simeq 6$ THz, and $G_{\text{int}} \simeq 100$ ℧/℧. Results are further corroborated analytically using the Wentzel-Kramers-Brillouin approximation and also benchmarked with previous reports. Furthermore, the effect of extrinsic parameters, such as Schottky barrier height and strain on f_t and $f_{\max}$, is discussed. This study can thus be used as a comprehensive, physics-based search guide of two-dimensional materials for radio-frequency applications.

DOI: 10.1103/PhysRevApplied.10.014022

I. INTRODUCTION

Low contact resistance, output current saturation, high mobility, and compatibility with CMOS processes are some of the most desirable properties for potential radio-frequency (rf) devices [1]. Silicon-on-insulator (SOI) FETs are promising for rf applications because of their easy manufacture using mainstream Si technology and improved short-channel effects [2–5]. However, the low mobility of silicon and performance degradation due to the increased role of surface roughness in the ultra-thin limit has deterred further improvements with transistor scaling [6]. At the same time, increasing bandwidths in communication systems and sensor applications [7] need devices with operating frequencies deep in the terahertz regime. Graphene with high mobility and saturation velocity has emerged as a prospective material for radio-frequency applications [8–11]. However, the lack of a bandgap limits its maximum oscillation frequency $f_{\max}$ (approximately 200 GHz for a gate length of 60 nm) due to high output conductance [12].

Two-dimensional (2D) layered semiconducting materials with their sizeable bandgap and remarkable electronic properties have seen significant research interest for radio-frequency applications [13,14]. Further, the potential to integrate 2D materials on low-cost flexible substrates is an additional advantage over high-cost SOI and III-V semiconductors [15,16]. The ultra-thin nature and the absence of dangling bonds in 2D materials make it possible to scale the FETs down to gate lengths as low as 1 nm [17]. Previous reports on 2D material-based rf devices using MoS_2 [18,19] and black phosphorus [20] have demonstrated unity current gain cutoff frequency (f_t) and $f_{\max}$ values in the deep GHz regime. In a recent simulation study, Yin *et al.* [21] predicted the intrinsic performance limit of phosphorene transistors by varying physical parameters such as channel length, effective oxide thickness (EOT) and contact resistance. However, a comprehensive study of the dependence of the two important rf figures of merit (FOM), i.e., f_t and $f_{\max}$, on channel material properties and hence the rf performance projections for different 2D materials is lacking in the current literature.

In this work, a physics-based atomistic simulation platform is developed to make high-frequency performance projections based on channel material properties such as effective mass, dielectric constant, and bandgap. These simulations are performed on a Schottky barrier metal-oxide-semiconductor FET (SB MOSFET) structure with a 15-nm gate length. The nonequilibrium Green's function (NEGF) formalism within the effective mass

---

[*] slodha@ee.iitb.ac.in

approach self-consistently coupled to Poisson's equation is employed in order to extract the important FOMs for rf applications. Transfer and output characteristics of the simulated devices are compared with previous reports to validate the simulations [22,23]. Further, the variations in f_t, $f_{\max}$ and the intrinsic gain (G_{int}) with effective mass (m^*) and dielectric constant (ϵ_r) are studied to develop a qualitative understanding of the dependence of the rf performance on material properties. Among the various 2D materials analyzed in this work covering a broad range of m^* and ϵ_r, including MoS_2, WS_2, WSe_2, and phosphorene, we find that phosphorene with a low m^* and high ϵ_r is the most promising 2D channel material with the highest f_t and $f_{\max}$. Further, the results are analytically validated using the Wentzel-Kramers-Brillouin (WKB) approximation and also benchmarked with previous work [22,23].

This paper begins by describing the methodology and equations used in developing the atomistic simulator. Next, the transistor characteristics are benchmarked to validate the simulation framework used in this work. Then, the important FOMs for various 2D channel materials are extracted and examined in detail. Finally, the paper concludes by summarizing the important results and discussing future scope.

II. METHODS

A schematic overview of the simulation framework is shown in Fig. 1. Various crucial parameters for rf performance such as bandgap, m^*, ϵ_r, thickness of the 2D channel material and the source and drain Schottky barrier heights (SBH) are given as inputs to the quantum ballistic simulator (QBS), as shown in Fig. 1(a). Bandgap, m^*, and ϵ_r values for different materials considered in this study are available in the Supplemental Material [24–26]. A Schottky barrier SOI transistor structure with 15-nm gate length [Fig. 1(b)] is simulated using the QBS for different channel materials. A monolayer of 2D material is sandwiched between the bottom (8-nm SiO_2) and the top oxide (2.8-nm HfO_2). These particular device dimensions are chosen to validate the QBS with a previous report [22]. Most metals form Schottky contacts when interfaced with the 2D materials studied in this work. However, large variation is seen in published reports of SBH values for the same metal on a particular 2D material as well as across various 2D materials. Because of this reason, and to ensure that the focus of this work is on evaluating rf performance for variations in intrinsic material properties (bandgap, m^*, ϵ_r), constant SBH values of 0.1 eV [22] are assumed at the source and drain contacts for all the materials analyzed in this work. However, we do show the dependence of f_t and $f_{\max}$ on SBH for specific bandgap, m^*, and ϵ_r values later in the paper (f_t) and also in the Supplemental Material ($f_{\max}$) [26]. Figure 1(c) depicts the schematic QBS output of the simulated devices, i.e., transfer (I_D-V_G) and output (I_D-V_D) characteristics at fixed drain bias (V_D) and gate bias (V_G), respectively. Three important figures of merit for rf devices (f_t, $f_{\max}$, and G_{int}) are extracted from the output and transfer characteristics. The quantities f_t and $f_{\max}$ are calculated using the following equations:

$$f_t = \frac{g_m}{2\pi C_G}, \tag{1}$$

$$f_{\max} = \frac{f_t}{2\sqrt{g_d(R_s + R_g W) + 2\pi f_t C_{GD} R_g W}}. \tag{2}$$

Here, the transconductance (g_m), the gate capacitance (C_G), the output conductance (g_d), and the gate-to-drain capacitance (C_{GD}) are extracted from the I_D-V_G and I_D-V_D characteristics at fixed $V_D = 0.9$ V, $V_G = 0.6$ V for a channel width of $W = 1$ μm. Typical values of width-normalized source contact resistance ($R_S = 500$ $\Omega\,\mu$m) and gate resistance-width product ($R_g W = 500$ $\Omega\,\mu$m) are used to calculate $f_{\max}$ [23]. The QBS solves the

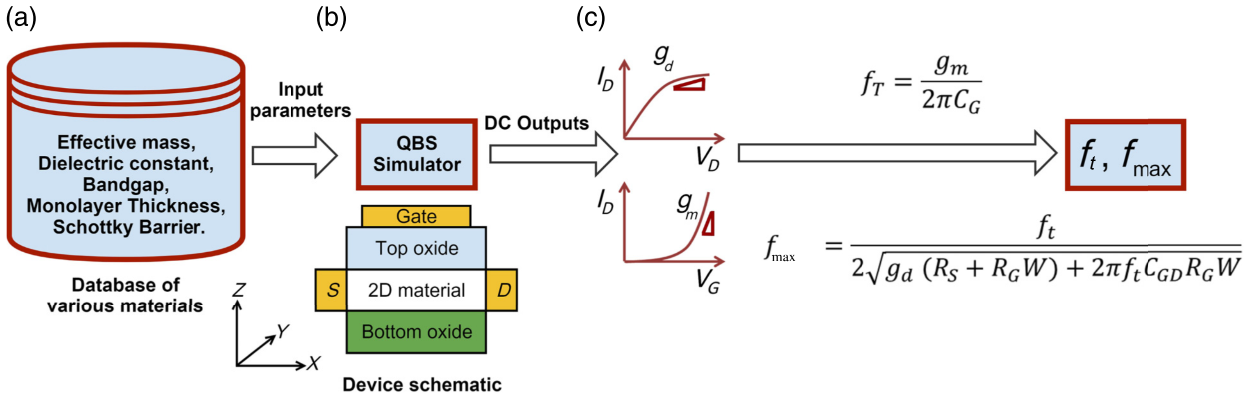

FIG. 1. Schematic overview of the QBS framework. (a) Database of various 2D materials taken as an input to the QBS. (b) Schematic of the Schottky barrier MOSFET simulated using the QBS. (c) Output conductance (g_d) and transconductance (g_m) extracted from I_D-V_D and I_D-V_G characteristics, ultimately used in calculating the f_t and $f_{\max}$.

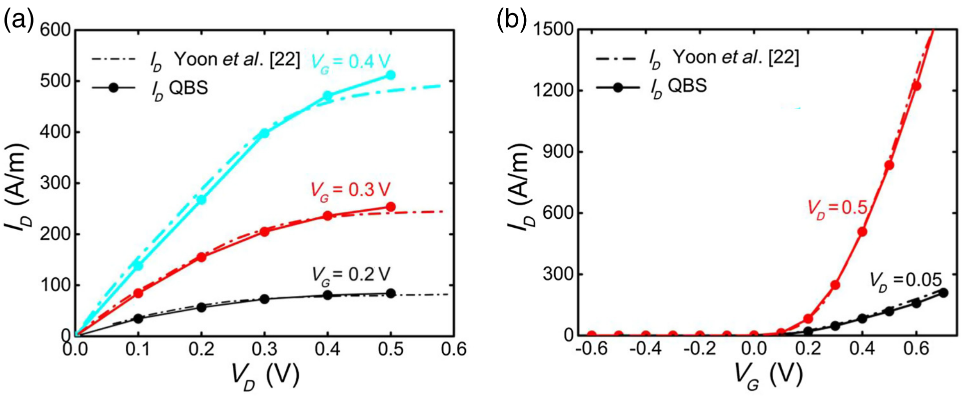

FIG. 2. (a),(b) Output and transfer characteristics obtained using QBS for a 15-nm gate length Schottky barrier FET with MoS_2 as the channel material. Simulated characteristics are benchmarked against published data [22].

one-dimensional [along the x direction, see Fig. 1(b)] NEGF equations within the effective mass Hamiltonian framework. It is important to note that electron wave functions are assumed not to extend into the bottom and top oxides due to the large barrier between the channel material and the oxides. Transport equations based on the NEGF formalism are solved self-consistently with Poisson's equation to extract the transfer and output characteristics. The transverse direction [y axis along the width of the channel in Fig. 1(b)] is taken into account by summing over transverse momentum modes (Fig. 1), such that, the drain to source current (I_D) is calculated using [22]

$$I_D = \frac{e}{\hbar}\sqrt{\frac{m_y^* k_B T}{2\pi^3}} \int dE_{k_x} \left\{ F_{-1/2}\left(\frac{\mu_1 - E_{k_x}}{k_B T}\right) - F_{-1/2}\left(\frac{\mu_2 - E_{k_x}}{k_B T}\right) \right\} T_{SD}(E_{k_x}), \qquad (3)$$

where $F_{-1/2}$ is the Fermi-Dirac integral of order $-1/2$ and the transmission coefficient (T_{SD}) is calculated from NEGF, μ_1 and μ_2 are the source and drain electrochemical potentials, $\hbar$, m_y^*, e, k_B, T, and E_{k_x} are the reduced Planck constant, transverse effective mass, elementary charge, Boltzmann's constant, temperature, and longitudinal energy, respectively. Gate leakage current is not considered in these simulations as it is negligible compared to the drain current at large gate and drain voltages [12]. Dirichlet boundary conditions are used at the contacts, and Neumann boundary conditions are applied at all material-air interfaces [12]. The source terminal is assumed to be grounded.

III. RESULTS AND DISCUSSION

To validate the QBS, the simulated I-V curves of a top gate MoS_2 transistor with a gate length of 15 nm and EOT of 0.44 nm are compared with a previous report [22]. Figures 2(a) and 2(b) show the output and transfer characteristics extracted from QBS and the previous work, respectively [22]. The results are in good agreement at small gate and drain voltages. A slight deviation in the output and transfer characteristics for larger gate voltages could possibly be from differences in device details such as the Fermi energy of the metal, the number of valleys considered, and the metal work function, which were not mentioned in the previous report [22]. In addition to the QBS validation, f_t for MoS_2 at fixed drain (0.4 V) and gate (0.4 V) voltages is calculated using Eq. (1). Results are further compared and validated with the analytical expression for f_t calculated using the $k \cdot p$ model which includes band-to-band tunneling (BTBT), as shown in Fig. 3(b) [23]. A decrease in the channel length leads to a shorter source-to-drain transit time, thereby increasing f_t. The slight overestimation in f_t extracted using QBS compared to the $k \cdot p$ model [23] is due to the absence of a BTBT model in QBS. The BTBT-assisted current

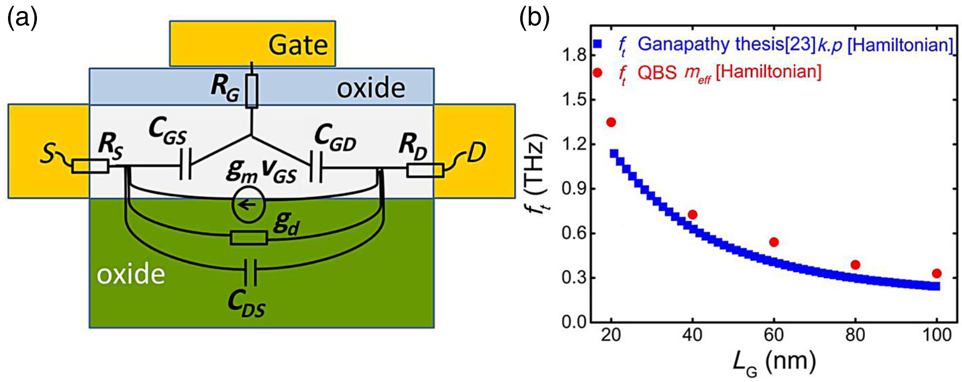

FIG. 3. (a) Various parasitic elements of the Schottky barrier FET crucial to high-frequency performance (i.e., f_t and $f_{\max}$). (b) Unity current gain cutoff frequency f_t calculated for monolayer MoS_2 channel from the $k \cdot p$ model [23] and the effective mass Hamiltonian used in this work.

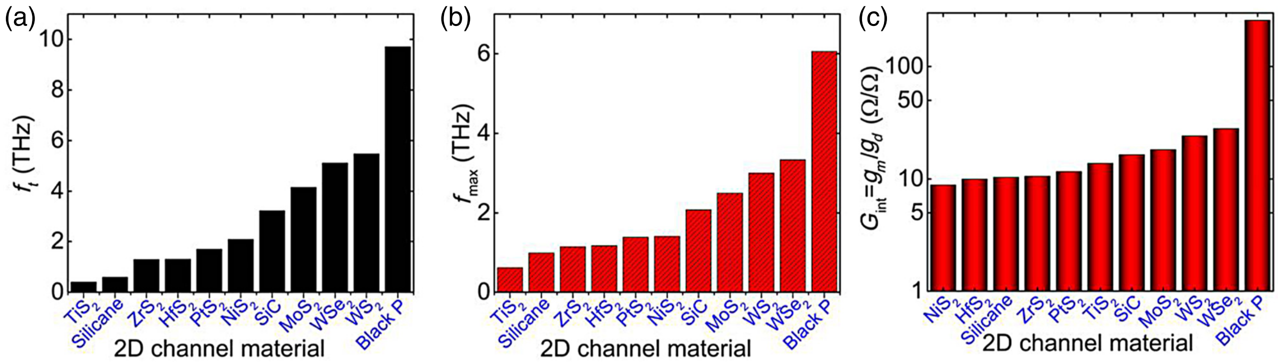

FIG. 4. Important FOMs for rf performance. (a) Cutoff frequency, (b) maximum oscillation frequency, and (c) intrinsic gain for various 2D channel materials.

reduces the transconductance and thus f_t. Various parasitics involved in f_t and f_{max} extraction are shown in Fig. 3(a). Besides MoS$_2$ we also simulate DC characteristics and rf performance for BP transistors using QBS and find the results to be in close agreement with recently published work [27]. This reinforces the credibility in QBS to be able to accurately predict the rf performance for a large variety of 2D materials.

We now extract f_t, f_{max}, and G_{int} for various 2D materials, namely, TiS$_2$, silicane, ZrS$_2$, HfS$_2$, PtS$_2$, NiS$_2$, SiC, MoS$_2$, WS$_2$, WSe$_2$, and phosphorene, as shown in Figs. 4(a)–4(c), respectively. The thickness of the channel material and the electron barrier height are kept constant, whereas the bandgap, m^* and ϵ_r are varied. A table for the material properties is given in the Supplemental Material. The highest f_t, f_{max}, and G_{int} values for phosphorene among the 2D materials considered here stems from its low m^* and high ϵ_r. Moreover, the f_t values are benchmarked with previous studies as shown in Table I. Almost a tenfold improvement in f_t in this work as compared to previous work [19,28,29] results from the lack of scattering in the channel. The presence of scattering in previous experimental and theoretical studies for long channel length transistors (>250 nm) limits the intrinsic f_t. Therefore, for the previous reports, we extrapolate the f_t for 15-nm gate length using $v_{\text{sat}} = L_g/\tau = 2\pi L_g f_t$ [19] and compare it with f_t reported in this work. Hence, f_t reported in this work can be considered as the intrinsic ballistic limit for a 15-nm gate length transistor. The higher f_t for phosphorene reported in this work compared to Yin *et al.* [21], can be attributed to the reduced EOT (0.44 vs 1.3 nm).

TABLE I. Unity current gain cutoff frequencies for monolayer transistors with different channel materials reported previously and in this work.

Channel material	Previous work		This work
	v_{sat} (cm/s)	f_t (THz) at 15 nm	f_t (THz) at 15 nm
MoS$_2$	4.8×10^6 [28]	0.51	4.15
	1.1×10^6 [19]	0.12	
	1.8×10^6 [29]	0.2	
WS$_2$	5.1×10^6 [28]	0.54	5.4
WSe$_2$	4×10^6 [28]	0.42	5.1
Phosphorene	9.6×10^6 [20]	1	9.7
	2.5×10^7 [21]	5	9.7

Further, f_t and f_{max} with varying m^* and ϵ_r are extracted to understand their trends for different channel materials (Fig. 4). Variations in f_t, f_{max}, and G_{int} with m^* and ϵ_r for a constant energy bandgap (1.5 eV) are shown in Figs. 5(a)–5(c), respectively. Solid yellow spheres in Fig. 5 represent various materials considering their specific bandgaps in the QBS. Almost all spheres lie on the same trend that houses the f_t and f_{max} variations for a constant bandgap. The fact that this trend is not dependent of the actual bandgap suggests a negligible effect of bandgap on f_t, f_{max}, and G_{int}. A small electronic barrier (0.1 eV) gives rise to a dominant electronic current through the conduction band and a negligible hole current for sizeable bandgap due to a large hole barrier. Reduction in bandgap lowers the hole barrier and below a critical value that depends on m^* and ϵ_r, the hole current increases and affects f_t and f_{max}. However, most of the monolayer 2D materials considered in this study have a bandgap above their respective critical bandgaps. Therefore, no considerable effect of bandgap on f_t and f_{max} is observed. A detailed analysis on the effect of bandgap on f_t and f_{max} is provided in the Supplemental Material [26]. Figures 5(a) and 5(b) show that lower m^* and higher ϵ_r lead to higher f_t and f_{max}. In these simulations, ϵ_r is varied from 1 to 15 and m^*/m_0 from 0.13 to 6 spanning a wide range of relevant 2D materials. Variations in f_t and f_{max} are attributed to the modulation of the source-channel barrier width and the DOS with m^* and ϵ_r. Detailed explanations of the effect of m^* and ϵ_r on f_t and f_{max} are presented in the following sections.

To understand the variation in f_t for different channel materials, we study the g_m and C_G trends for varying m^*

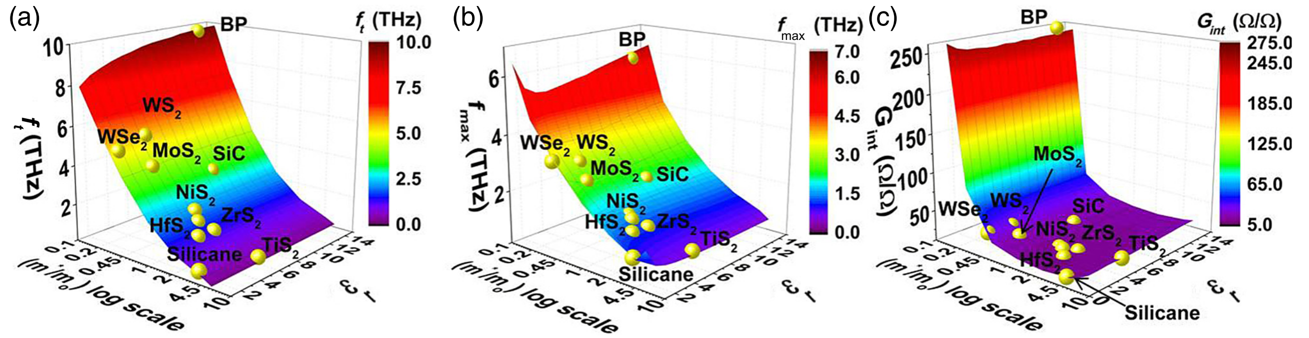

FIG. 5. (a) f_t, (b) $f_{\max}$, and, (c) G_{int} with varying m^*/m_0 and ϵ_r for a constant energy bandgap of 1.5 eV. Yellow spheres represent the various channel materials with their respective bandgaps.

and ϵ_r, since f_t depends on these two crucial parameters. Figure 6(a) depicts a significant variation in f_t with m^*, but only a small variation with ϵ_r. First, consider the effect of ϵ_r on f_t for constant m^*. f_t varies with ϵ_r only for small m^* and remains nearly constant for larger values of m^*. Therefore, normalized f_t along the α-α' curve shown in Fig. 6(a) is plotted for small and constant m^* (m^*/m_0 = 0.13) in Fig. 6(b). Figure 6(b) shows f_t increasing monotonically for increasing ϵ_r. We further look at the variation of g_m and C_G with ϵ_r for constant m^*/m_0 = 0.13. Both g_m and C_G increase up to a certain ϵ_r and then start decreasing for higher ϵ_r, as shown in Fig. 6(c). However, since their ratio continues increasing monotonically with ϵ_r, f_t also increases monotonically with ϵ_r [Fig. 6(b)]. The initial increase in both g_m and C_G is attributed to the improved effective gate control of the source-channel barrier for ϵ_r increasing up to a value of approximately 5 [30]. However, a further increase in ϵ_r reduces both g_m and C_G due

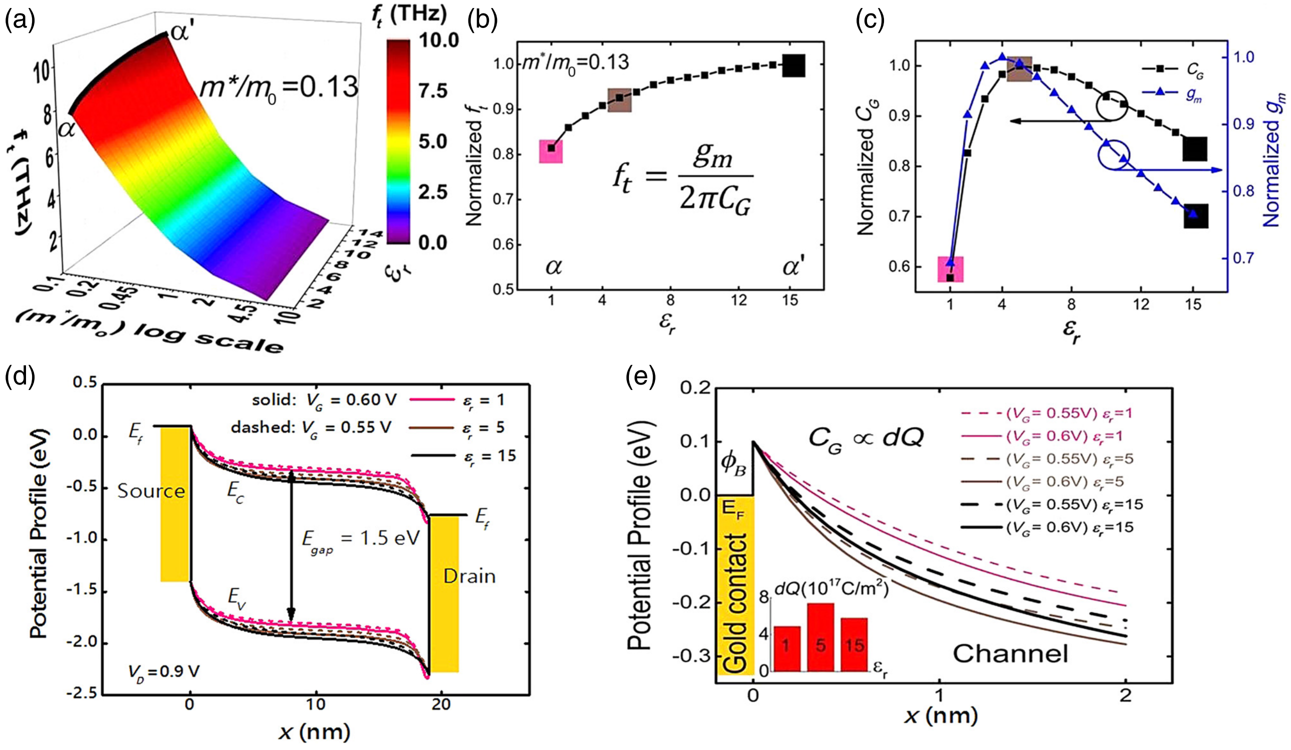

FIG. 6. (a) 3D f_t phase diagram for varying m^*/m_0 and ϵ_r. (b) Normalized f_t vs ϵ_r at constant $m^*/m_0 = 0.13$. Initially f_t increases fast with ϵ_r due to increased gate-to-channel coupling. A further increase in $\epsilon_r > 5$ leads to enhanced drain control over the source-channel barrier that dominates over the gate-to-channel coupling. (c) Normalized C_G and g_m for varying ϵ_r. (d) Energy band diagrams along the channel for different $\epsilon_r = 1$, 5, 15 and gate voltages (0.55 and 6 V) show the bands shifting downwards (thinner barrier) for ϵ_r increasing from 1 to 5 but pulled up by the drain (thicker barrier) for $\epsilon_r > 5$. (e) Conduction band profiles near the source end. Change in total charge (dQ) for a 50 mV change in the gate voltage and for different ϵ_r is shown in the inset.

to more dominant drain coupling to the source-channel barrier [31]. Figures 6(d) and 6(e) show the barrier width modulation at the source-channel interface for various ϵ_r values at different drain voltages. Device performance at high drain voltage is largely dependent on the source-channel barrier due to negligible contribution to I_D from the drain contact. The conduction band profiles of Fig. 6(d) are magnified near the source-channel interface to understand barrier width variation with V_G and ϵ_r, as shown in Fig. 6(e). The change in conduction band profiles for V_G varying from 0.55 to 0.6 V determines the change in channel charge [inset of Fig. 6(e)]. This change in charge represents C_G $(= dQ_{\text{ch}}/dV_g)$ and is consistent with the C_G trend depicted in Fig. 6(c). Further, the variation in conduction band profiles is also consistent with the g_m trend in Fig. 6(c) and explained in detail via Fig. 7. Figure 7(a) depicts the electric field lines emanating from the gate and drain for three different ϵ_r values (1, 5, and 15). The field strength from the gate to the source increases for an initial increase in ϵ_r (higher density of gate field lines) from 1 to 5 resulting in improved gate control, a thinner source-channel barrier and thus a higher g_m. With further increase in $\epsilon_r > 5$, the field lines from the drain start affecting the source-channel barrier, resulting in the barrier becoming wider and hence reducing g_m [31]. Figure 7(b) shows the conduction band profiles for these three ϵ_r conditions. An initial increase in ϵ_r shifts the bands down [from the pink to the brown profile in Fig. 7(b)] due to a high gate field effect and a further increase in ϵ_r pulls the bands in the channel towards the drain (brown to black) due to a strong drain field. These results are also validated using the WKB analytic approximation, [32] using a factor F_G proportional to g_m, as plotted in the inset of Fig. 7(c). The factor F_G is given by

$$F_G = -I\left(\frac{2}{W_B} + \frac{\sqrt{m^*}}{C}\right)\frac{dW_B}{dV_G}, \tag{4}$$

where C is a constant independent of channel material parameters, W_B is the width of the barrier at source Fermi level as obtained from simulations, dW_B is the change in W_B for the dV_G voltage bias change, and I is the drain-to-source current. The above calculation results from the WKB approximation assuming that the current is being controlled by a triangular source-channel barrier. An increase in F_G for an initial increase in ϵ_r (1 to 5) can be attributed to reduction in W_B and increased dW_B/dV_G [inset of Fig. 7(c)]. A further increase in ϵ_r (5 to 15) increases W_B and reduces dW_B/dV_G, thereby reducing F_G. The variation in F_G is in complete agreement with the g_m vs ϵ_r trend shown in Fig. 6(c). Detailed information about F_G is given in the Supplemental Material [26]. The variation in f_t with m^* is more pronounced, as shown in Fig. 8. For a constant ϵ_r, f_t along the β-β' curve of Fig. 8(a) decreases monotonically with an increase in m^* [Fig. 8(b)]. Figure 8(c) shows the change in g_m and C_G with m^* with an equivalent gate capacitance model in the inset. As detailed in [33], this capacitance model represents the intrinsic behavior of any semiconductor material including the quantum capacitance (C_Q). An increase in the normalized C_G with m^* results from increasing C_Q due to an increased DOS for large m^*. However, g_m decreases due to reduced gate-assisted tunneling at the source-channel barrier resulting from degrading gate

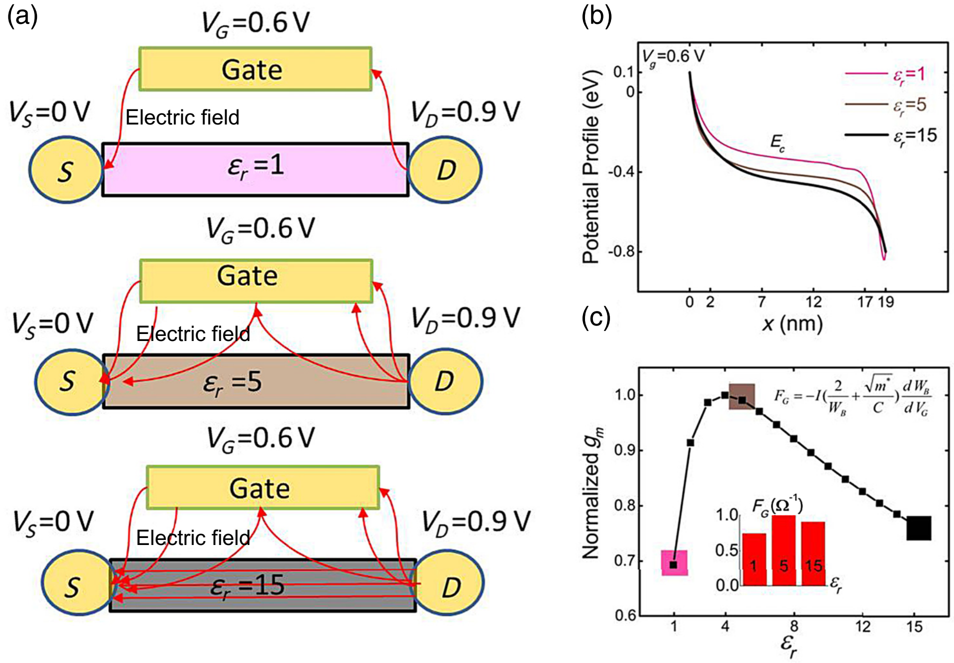

FIG. 7. (a) Electric field lines for varying ϵ_r of the channel material. An increase in ϵ_r from 1 to 5 allows electric field lines to travel deeper inside the channel, thereby improving the gate control of the source-channel barrier. A further increase in ϵ_r deteriorates the gate control due to an increase in the drain field at the source. Electric field lines flow from drain to source through the channel for higher ϵ_r. (b) Conduction energy band profiles from source to drain at $V_D = 0.9$ V and $V_G = 0.6$ V for different ϵ_r. (c) Normalized g_m for varying ϵ_r. Initial increase in ϵ_r from 1 to 5 increases the g_m due to better gate control, a further increase in ϵ_r from 5 to 15 reduces the g_m because of the increase in drain-to-source coupling. Factor F_G (in the inset) shows the same variation as g_m.

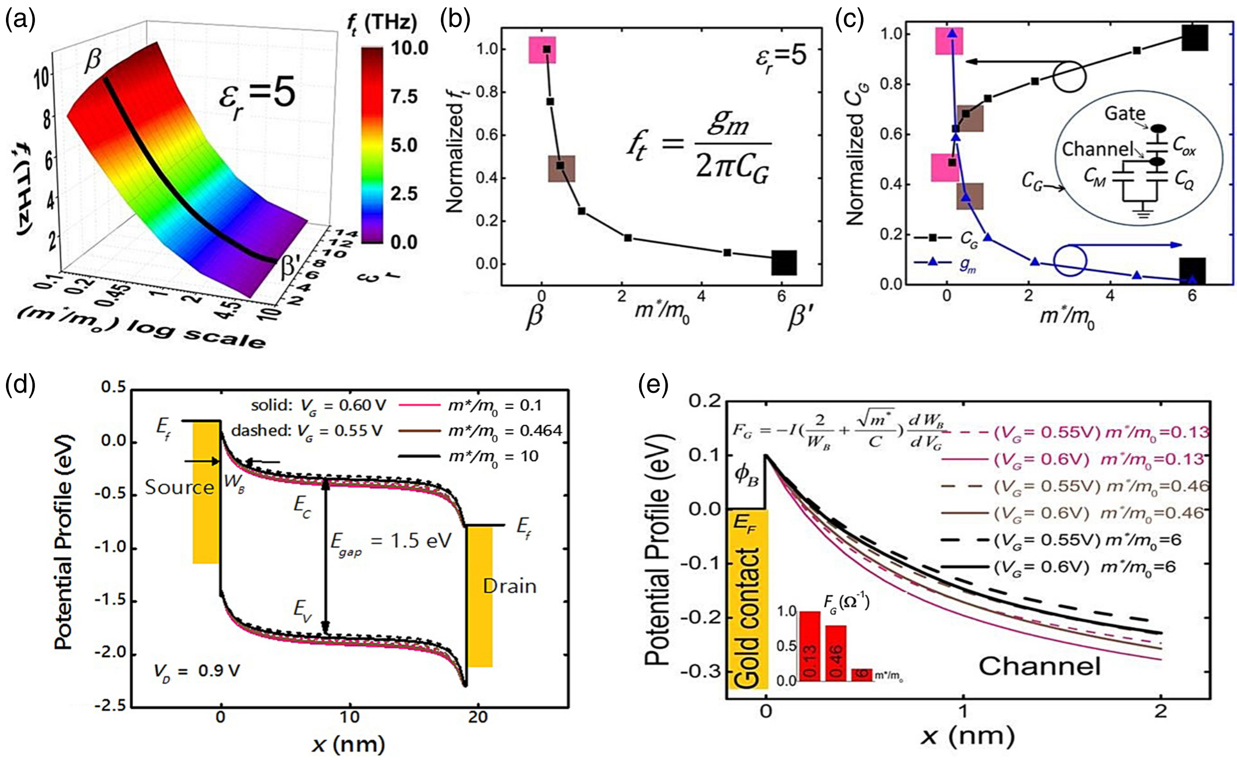

FIG. 8. (a) 3D f_t phase diagram for varying m^*/m_0 and ϵ_r. (b) Normalized f_t vs m^*/m_0 at constant $\epsilon_r = 5$. We note that f_t decreases monotonically with increasing m^* due to an increase in the DOS leading to a reduction in the gate capacitance. (c) Normalized C_G and g_m vs m^*/m_0 showing a decrease in the gate capacitance with increasing m^* as the gate capacitance can be modeled [33] using oxide capacitance in series with a parallel combination of the material capacitance and the quantum capacitance (C_Q) shown in the inset. The quantum capacitance is directly proportional to the DOS and, C_M, the material capacitance is directly proportional to ϵ_r. (d) Energy band diagrams from source to drain for different V_G (0.55 and 0.6 V) and m^*/m_0 (0.13, 0.46, 6). (e) Magnified conduction band profile near the source end shows that the bands shift upward with m^* leading to a reduction in g_m. In the inset, the analytical WKB factor F_G, which is proportional to g_m, reveals the same trend as shown by g_m.

control of the source-channel barrier with increasing m^* [34]. Energy band profiles for different m^* (0.13, 0.46, and 6) and for different V_G are shown in Fig. 8(d). Figure 8(e) shows the enlarged conduction band profiles near the source, where besides widening of the source-channel barrier, the gate-assisted change in the conduction band profile decreases with increasing m^* leading to a reduction in g_m. Further, the analytical WKB factor F_G plotted for different m^* is in agreement with the g_m trend, as shown in the inset of Fig. 8(e). The decrease in F_G with m^* can be attributed to reduction in dW_B/dV_G, $1/W_B$, and I for increasing m^*.

Another important FOM for rf applications is the maximum oscillation frequency $f_{\max}$. Variations in $f_{\max}$ with m^*/m_0 and ϵ_r are depicted in Fig. 9. We notice that similar to f_t, $f_{\max}$ is also a strong function of m^*. First, we look at the change in $f_{\max}$ by varying ϵ_r for a constant $m^*/m_0 = 0.13$. The normalized $f_{\max}$ and f_t along the α-α' curve in Fig. 9(a) with varying ϵ_r are shown in Fig. 9(b). Unlike f_t, which is monotonically increasing, $f_{\max}$ initially decreases with ϵ_r and then increases for higher values of $\epsilon_r > 5$. As shown in Eq. (2), besides f_t, $f_{\max}$ also depends on g_d, C_{GD}, etc. which in turn depend on ϵ_r. Figure 9(c) shows that g_d increases initially with ϵ_r and then decreases for $\epsilon_r > 5$. Similar to g_d, C_{GD} and f_tC_{GD} also follow a similar trend, i.e., both initially increase and then decrease for larger values of ϵ_r, as seen in Fig. 9(d). A factor F_D proportional to g_d is plotted for three different ϵ_r and is shown in the inset of Fig. 9(c). The factor F_D, also derived from WKB approximation, is given by,

$$F_D = -I\left(\frac{2}{W_B} + \frac{\sqrt{m^*}}{C}\right)\frac{dW_B}{dV_D}, \tag{5}$$

where dW_B/dV_D is the change in W_B for dV_D. The variation in F_D, similar to F_G, can be explained by an initial increase in $1/W_B$ and dW_B/dV_D for ϵ_r increasing from 1 to 5 due to improved gate-channel coupling and reduction in $1/W_B$ and dW_B/dV_D for ϵ_r increasing from 5 to 15 due to increased drain-to-channel coupling. The variations in g_d, C_{GD}, and f_tC_{GD} with ϵ_r can be explained by barrier width modulation at the source-channel interface, as shown in Figs. 6(e) and 9(e). An initial increase in ϵ_r strengthens the gate control due to an increasing density of field lines from the gate to the source-channel barrier; hence resulting in an increase in g_d, gate to drain capacitance (C_{GD}), and f_tC_{GD}. A further increase in ϵ_r reduces the gate control, as the field lines from the drain are more strongly coupled to the source-channel barrier resulting in a wider barrier width and a reduction in g_d, C_{GD}, and f_tC_{GD} [Fig. 9(d)]. Figure 9(e) shows the variation in the conduction band profiles from source to drain as ϵ_r and V_D are varied. An increase in the barrier width due to the conduction band floating up for very large ϵ_r results in a reduction in g_d. The inset in Fig. 9(e) shows the variation of charge integrated from the drain contact to the middle of the channel, which corresponds to the C_{GD} variation shown in Fig. 9(d). The C_{GD} is extracted by assuming that the left half of the channel is controlled by the source whereas the right half is controlled by the drain (α = 0.5). Here, α is defined as the ratio of length of the source-controlled channel to the total channel length. Figure 4 in the Supplemental Material [26] shows that even a large change in α from 0.1 to 0.5 does not affect $f_{\max}$ for phosphorene significantly.

The variation in $f_{\max}$ with m^* is shown in Fig. 10. Similar to f_t, $f_{\max}$ decreases monotonically with an increase in m^* along the β-β' curve shown in Fig. 10(a) for a constant $\epsilon_r = 5$. Figure 10(b) shows the normalized f_t and $f_{\max}$ for varying m^* at a constant ϵ_r. As discussed earlier, $f_{\max}$ depends strongly on g_d and C_{GD}. Figure 10(c) shows that g_d initially increases for low m^* and then decreases for high m^*. A very low m^* makes the source-channel barrier almost transparent to carriers and the significant tunneling implies reduced drain control and low g_d. However, with increasing m^* the current becomes more sensitive to the drain voltage due to reduced tunneling, thereby increasing g_d. A further increase in m^*/m_0 (>0.46) leads to a larger DOS, along with which the conduction band also floats up as shown in Fig. 10(e) (increasing the difference between E_F and E_C near the source). This increase in barrier width due to the conduction band floating up in turn reduces the drain control over the source-channel barrier and leads to a reduction in g_d. Unlike F_G, the factor F_D [inset of Fig. 10(c)] initially increases due to an increase in $\sqrt{m^*}/C$ and then decreases due to a decrease in $1/W_B$ and dW_B/dV_D resulting from the increased DOS. The trend depicted by factor F_D is in complete agreement with the g_d vs m^* trend in Fig. 10(c). Figure 10(d) shows that C_{GD} increases with m^*/m_0 due to the increase in DOS

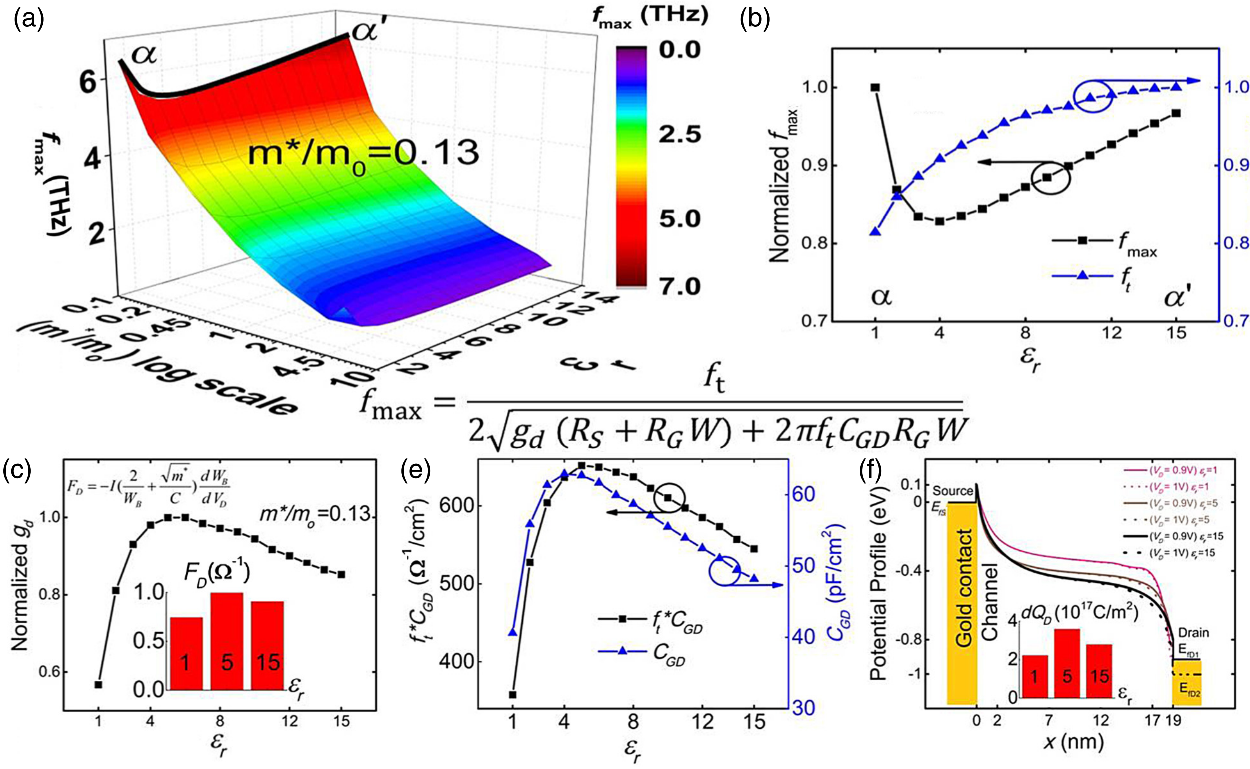

FIG. 9. (a) Phase diagram showing the change in $f_{\max}$ with m^*/m_0 and ϵ_r. (b) Normalized $f_{\max}$ and f_t vs ϵ_r at constant $m^*/m_0 = 0.13$. (c) g_d vs ϵ_r shows that initially g_d increases and then decreases with ϵ_r. In the inset, the analytical WKB factor F_D proportional to g_d shows a similar variation as g_d at different ϵ_r. (d) Plot of f_tC_{GD} and C_{GD} vs ϵ_r. (e) Conduction band diagrams showing the variation with ϵ_r for different V_D. In the inset, Q_D-ϵ_r variations are shown for a 50 mV change in the drain voltage bias that are consistent with the C_{GD} trends in (d).

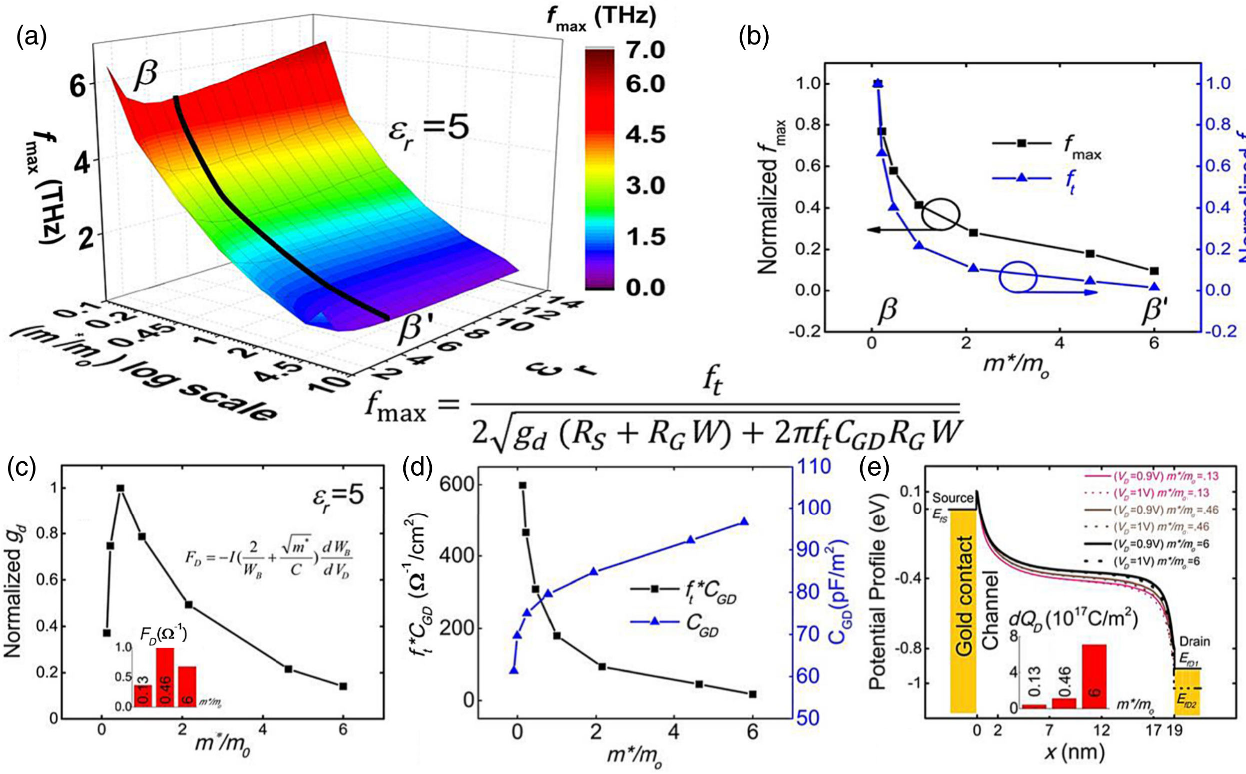

FIG. 10. (a) 3D $f_{\max}$ phase diagram for varying m^*/m_0 and ϵ_r. (b) Normalized $f_{\max}$ and f_t vs m^*/m_0 at constant $\epsilon_r = 5$. (c) g_d vs m^*/m_0 shows initially g_d increases and then decreases with m^*/m_0. Inset shows analytical WKB factor F_D showing similar variation as g_d. (d) Variation of C_{GD} and $f_t C_{GD}$ for varying m^*/m_0. (e) Energy band diagrams for different m^*/m_0 and at different drain voltages. Inset shows Q_D variation with m^*/m_0 for 50 mV change in drain voltage.

for high values of m^*/m_0. However, $f_t C_{GD}$ decreases with an increase in m^*/m_0 due to a strong dependence of f_t on m^*. Figure 10(e) shows the conduction band energy profiles for various m^*/m_0 at different drain voltages and the inset shows corresponding Q_D variation consistent with the C_{GD} trend in Fig. 10(d).

IV. EFFECT OF SCHOTTKY BARRIER HEIGHT AND STRAIN ON f_t

In this section, we briefly discuss the effects of variation in extrinsic parameters such as SBH and strain. The effective SBH for MoS_2 can be controlled either by interfacial engineering or chemical doping [35,36]. This analysis is performed for the best performing material (phosphorene), but similar arguments can be made for other 2D materials as well.

Figure 11(a) shows the trends in g_m, C_G, and f_t with varying electron SBH (ϕ_B) for phosphorene. f_t decreases monotonically with increasing SBH due to a reduction in g_m resulting from the increasing contact resistance. In addition, the effect of strain on rf performance is also of interest from the viewpoint of flexible electronics. Figure 11(b) shows the change in f_t for phosphorene under different

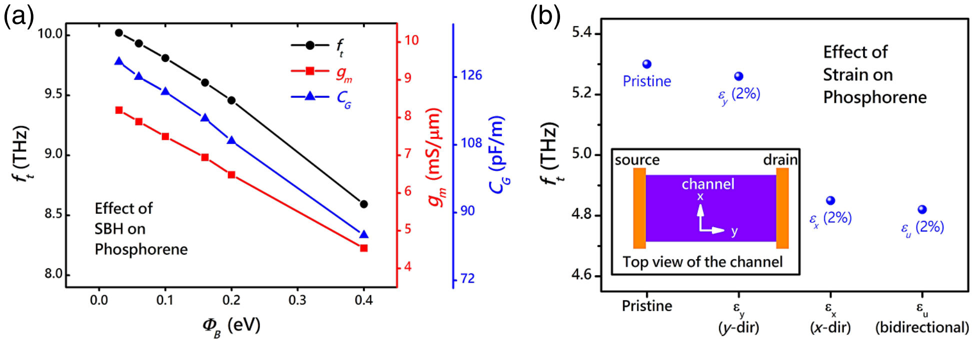

FIG. 11. (a) Variation in g_m, C_G, and f_t with SBH for phosphorene. (b) Effect of strain on f_t for phosphorene with SBH of 0.1 eV.

strain conditions with a fixed SBH of 0.1 eV. Values for the bandgap and directional electron and hole effective masses for phosphorene under strain are obtained from [37] and available in the Supplemental Material [26]. The inset in Fig. 11(b) shows the top view of the simulated device with indicated directions for strain. The effective mass in y direction is used as the transport effective mass whereas effective mass in x direction is used to calculate the transverse modes available for current transport, and hence both affect the f_t performance. Pristine phosphorene gives the best f_t performance and the effect of effective mass in x direction on f_t is found to be more significant when compared to the effective mass in the y direction. Similar analysis for $f_{\max}$ is available in the Supplemental Material [26].

V. CONCLUSIONS

This work reports a comprehensive study of the rf performance of 2D materials and identifies the contributions of different intrinsic material properties to standard rf FOMs, namely, f_t and $f_{\max}$. Unlike conventional bulk semiconductors, 2D materials offer the benefit of controllably scaling channel thickness. Superior electrostatics in sub–1-nm 2D monolayers can enable gate-length scaling for enhanced rf performance. Reduced scattering due to the absence of dangling bonds in pristine 2D materials can also benefit rf performance in comparison to conventional rf semiconductors. In addition, high mechanical stability under strain and optical transparency make 2D materials suitable for flexible and wearable rf electronics [38]. By analyzing the variation in m^* and ϵ_r and their effect on f_t, $f_{\max}$, and G_{int}, we demonstrate that a lower m^* and higher ϵ_r provide the best combination for rf applications. We demonstrate that this is due to the high degree of gate control over the source-channel barrier. An increase in the DOS for larger effective masses m^* reduces the modulation of the potential in the channel resulting in a poorer gate control. In the chosen set of materials, phosphorene emerges as the best material for rf applications due to its low m^* and high ϵ_r. Although not comprehensive, the list of 2D materials studied in this work covers a broad range of m^* and ϵ_r to enable performance predictions for other, known and yet to be discovered, 2D materials covered by it. Hence, this study could work as a guide for choosing specific materials for rf applications. To establish the credibility of our analysis, we also repeated the simulations for parameter (m^*, bandgap) values obtained by the *GW* method (see the Supplemental Material) [26]. It is important to note that the rf performance predicted in these simulations requires significant experimental improvements in (i) scaling gate dielectric thickness [25-nm Al_2O_3 (EOT approximately 10 nm) in [38] vs 2.8-nm HfO_2 (EOT approximately 0.44 nm) in this work], as well as (ii) scaling gate length from 100s of nm in recent experimental rf reports to 15 nm in this work. Another critical challenge is to develop techniques for improving the air stability of 2D materials, phosphorene in particular [39,40], since material degradation in ambient air can lead to loss of rf performance. Although the simulations account for contact resistance of the Schottky source and drain contacts, reduction in contact resistance through source and drain doping and/or metal work-function engineering can also help improve rf performance. From a simulation perspective, as a future extension of this work, the effect of scattering on f_t can be studied via the use of the incoherent NEGF formalism and the impact of extrinsic parameters related to device processing on rf performance, such as the Schottky barrier height, strain, and the substrate, can be looked at in more detail.

ACKNOWLEDGEMENT

This work was carried out at the IIT Bombay high-performance computing lab. We acknowledge funding support from the Ministry of Electronics and Information Technology (MeitY) and the Department of Science and Technology, Government of India. We also appreciate efforts by Akash Saini (akashsaini163@gmail.com) and Ankit Agarwal (ankitagarwal.316@gmail.com) in developing the codes used in this work.

[1] F. Schwierz, Graphene transistors: Status, prospects, and problems, Proc. IEEE **101**, 1567 (2013).

[2] H.-C. Yuan, G. K. Celler, and Z. Ma, 7.8-GHz flexible thin-film transistors on a low-temperature plastic substrate, J. Appl. Phys. **102**, 034501 (2007).

[3] G. Qin, L. Yang, J.-H. Seo, H.-C. Yuan, G. K. Celler, J. Ma, and Z. Ma, Experimental characterization and modeling of the bending strain effect on flexible microwave diodes and switches on plastic substrate, Appl. Phys. Lett. **99**, 243104 (2011).

[4] H. C. Yuan, M. M. Kelly, D. E. Savage, M. G. Lagally, G. K. Celler, and Z. Ma, Thermally processed high-mobility MOS thin-film transistors on transferable single-crystal elastically strain-sharing Si/SiGe/Si nanomembranes, IEEE Trans. Electron Devices **55**, 810 (2008).

[5] L. Sun, G. Qin, J.-H. Seo, G. K. Celler, W. Zhou, and Z. Ma, 12-GHz thin-film transistors on transferrable silicon nanomembranes for high-performance flexible electronics, Small **6**, 2553 (2010).

[6] Z. Ma, Y. H. Jung, J. H. Seo, J. Lee, S. J. Cho, T. H. Chang, H. Zhang, S. Gong, and W. Zhou, in *2016 China Semiconductor Technology International Conference (CSTIC), Shanghai, China* (2016), pp. 1–4.

[7] K. Kikuchi, *High Spectral Density Optical Communication Technologies*, Optical and Fiber Communications Reports Vol. 6 (Springer, 2010), pp. 11.

[8] K. Bolotin, K. Sikes, Z. Jiang, M. Klima, G. Fudenberg, J. Hone, P. Kim, and H. Stormer, Ultrahigh electron mobility in suspended graphene, Solid State Commun. **146**, 351 (2008).

[9] F. Schwierz, Graphene transistors, Nat. Nanotechnol. **5**, 487 (2010).

[10] V. E. Dorgan, M.-H. Bae, and E. Pop, Mobility and saturation velocity in graphene on SiO_2, Appl. Phys. Lett. **97**, 082112 (2010).

[11] V. E. Dorgan, A. Behnam, H. J. Conley, K. I. Bolotin, and E. Pop, High-field electrical and thermal transport in suspended graphene, Nano Lett. **13**, 4581 (2013).

[12] Z. Ren, Nanoscale MOSFETs: Physics, Simulation and Design (2006).

[13] N. Kaushik, A. Nipane, F. Basheer, S. Dubey, S. Grover, M. M. Deshmukh, and S. Lodha, Schottky barrier heights for Au and Pd contacts to MoS_2, Appl. Phys. Lett. **105**, 113505 (2014).

[14] G. Fiori, F. Bonaccorso, G. Iannaccone, T. Palacios, D. Neumaier, A. Seabaugh, S. K. Banerjee, and L. Colombo, Electronics based on two-dimensional materials, Nat. Nano **9**, 768 (2014).

[15] F. Torrisi and J. N. Coleman, Electrifying inks with 2D materials, Nat. Nano **9**, 738 (2014).

[16] Y. D. Kim and J. Hone, Materials science: Screen printing of 2D semiconductors, Nature **544**, 167 (2017).

[17] S. B. Desai, S. R. Madhvapathy, A. B. Sachid, J. P. Llinas, Q. Wang, G. H. Ahn, G. Pitner, M. J. Kim, J. Bokor, C. Hu, H.-S. P. Wong, and A. Javey, MoS_2 transistors with 1-nanometer gate lengths, Science **354**, 99 (2016).

[18] K. D. Holland, A. U. Alam, N. Paydavosi, M. Wong, C. M. Rogers, S. Rizwan, D. Kienle, and M. Vaidyanathan, Impact of contact resistance on the f_T and $f_{\max}$ of graphene versus MoS_2 transistors, IEEE Trans. Nanotechnol. **16**, 94 (2017).

[19] A. Sanne, R. Ghosh, A. Rai, M. N. Yogeesh, S. H. Shin, A. Sharma, K. Jarvis, L. Mathew, R. Rao, D. Akinwande, and S. Banerjee, Radio frequency transistors and circuits based on CVD MoS_2, Nano Lett. **15**, 5039 (2015).

[20] H. Wang, X. Wang, F. Xia, L. Wang, H. Jiang, Q. Xia, M. L. Chin, M. Dubey, and S.-j. Han, Black phosphorus radio-frequency transistors, Nano Lett. **14**, 6424 (2014).

[21] D. Yin, A. AlMutairi, and Y. Yoon, Assessment of high-frequency performance limit of black phosphorus field-effect transistors, IEEE Trans. Electron. Devices **99**, 1 (2017).

[22] Y. Yoon, K. Ganapathi, and S. Salahuddin, How good can monolayer MoS_2 transistors be? Nano Lett. **11**, 3768 (2011).

[23] K. Ganapathi, Ph.D. thesis, EECS Department, University of California, Berkeley, 2013.

[24] F. A. Rasmussen and K. S. Thygesen, Computational 2D materials database: Electronic structure of transition-metal dichalcogenides and oxides, J. Phys. Chem. C **119**, 13169 (2015).

[25] P. Miro, M. Audiffred, and T. Heine, An atlas of two-dimensional materials, Chem. Soc. Rev. **43**, 6537 (2014).

[26] See Supplemental Material at https://link.aps.org/supplemental/10.1103/PhysRevApplied.10.014022 for the detailed derivation of factors F_G and F_D, various material parameters, f_t and $f_{\max}$ results for material parameters obtained by the *GW* method and their comparison with the results reported in the main manuscript, α vs $f_{\max}$, effect of Schottky barrier height and strain on $f_{\max}$ performance of phosphorene and a detailed analysis of the dependence of f_t and $f_{\max}$ on the bandgap.

[27] Z. Yin, H. Li, H. Li, L. Jiang, Y. Shi, Y. Sun, G. Lu, Q. Zhang, X. Chen, and H. Zhang, Single-layer MoS_2 phototransistors, ACS Nano **6**, 74 (2012).

[28] Z. H. Jin, X. D. Li, J. T. Mullen, and K. W. Kim, Intrinsic transport properties of electrons and holes in monolayer transition-metal dichalcogenides, Phys. Rev. B **90**, 045422 (2014).

[29] R. Cheng, S. Jian, Y. Chen, N. Weiss, H. C. Cheng, H. Wu, Y. Huang, and X. Duan, Few-layer molybdenum disulfide transistors and circuits for high-speed flexible electronics, Nat. Commun. **5**, 5143 (2014).

[30] N. T. Rouf, A. H. Deep, R. B. Hassan, S. A. Khan, M. Hasan, and S. M. Mominuzzaman, High dielectric material dependence of carbon nanotube field effect transistor considering non-ballistic conduction, IET Micro Nano Lett. **9**, 620 (2014).

[31] J. Chang, L. F. Register, and S. K. Banerjee, Ballistic performance comparison of monolayer transition metal dichalcogenide MX_2 (M = Mo, W; X = S, Se, Te) metal-oxide-semiconductor field effect transistors, J. Appl. Phys. **115**, 084506 (2014).

[32] D. Ng Keh Ting, Ph.D. thesis, National University of Singapore, Electrical and computer Engineering, 2008. Appendix A.

[33] S. Luryi, Quantum capacitance devices, Appl. Phys. Lett. **52**, 501 (1988).

[34] K. Alam and R. K. Lake, Monolayer - transistors beyond the technology road map, IEEE Trans. Electron Devices **59**, 3250 (2012).

[35] N. Kaushik, D. Karmakar, A. Nipane, S. Karande, and S. Lodha, Interfacial n-doping using an ultrathin TiO_2 layer for contact resistance reduction in MoS_2, ACS Appl. Mater. Interfaces **8**, 256 (2015).

[36] A. Nipane, D. Karmakar, N. Kaushik, S. Karande, and S. Lodha, Few-layer MoS_2 p-type devices enabled by selective doping using low energy phosphorus implantation, ACS Nano **10**, 2128 (2016).

[37] Y. Li, S. Yang, and J. Li, Modulation of the electronic properties of ultrathin black phosphorus by strain and electrical field, J. Phys. Chem. C **118**, 23970 (2014).

[38] W. Zhu, S. Park, M. N. Yogeesh, K. M. McNicholas, S. R. Bank, and D. Akinwande, Black phosphorus flexible thin film transistors at Gighertz frequencies, Nano Lett. **16**, 2301 (2016).

[39] Y. Abate, D. Akinwande, S. Gamage, H. Wang, M. Snure, N. Poudel, and S. B. Cronin, Recent progress on stability and passivation of black phosphorus, Adv. Mater. 1704749 (2018).

[40] N. Goyal, N. Kaushik, H. Jawa, and S. Lodha, Enhanced stability and performance of few-layer black phosphorus transistors by electron beam irradiation, Nanoscale **10**, 11616 (2018).